Visualization and suppression of interfacial recombination for high-efficiency large-area pin perovskite solar cells

Martin Stolterfoht[1,+,*], Christian M. Wolff[1,+], José A. Márquez[2,*], Shanshan Zhang[1,3], Charles J. Hages[2], Daniel Rothhardt[1], Steve Albrecht[4], Paul L. Burn[3], Paul Meredith[5], Thomas Unold[2,*], Dieter Neher[1,*]

[+] *The first two authors contributed equally*

[1]Institute of Physics and Astronomy, University of Potsdam, Karl-Liebknecht-Str. 24-25, D-14476 Potsdam-Golm, Germany.

[2]Department of Structure and Dynamics of Energy Materials, Helmholtz-Zentrum-Berlin, Hahn-Meitner-Platz 1, D-14109 Berlin, Germany

[3]Centre for Organic Photonics & Electronics (COPE), School of Chemistry and Molecular Biosciences, The University of Queensland, Brisbane, QLD 4072, Australia

[4]Young Investigator Group Perovskite Tandem Solar Cells, Helmholtz-Zentrum Berlin für Materialien und Energie GmbH, Kekuléstraße 5, 12489 Berlin, Germany

[5]Department of Physics, Swansea University, Singleton Park, SA2 8PP Wales, United Kingdom

E-mail: stolterf@uni-potsdam.de, unold@helmholtz-berlin.de, neher@uni-potsdam.de

Abstract

The performance of perovskite solar cells (PSCs) is predominantly limited by non-radiative recombination, either through trap-assisted recombination in the absorber layer or *via* minority carrier recombination at the perovskite/transport layer interfaces. Here we use transient and absolute photoluminescence imaging to visualize all non-radiative recombination pathways in planar *pin*-type PSCs with undoped organic charge transporting layers. We find significant quasi-Fermi level splitting losses (135 meV) in the perovskite bulk, while interfacial recombination results in an additional free energy loss of 80 meV at each individual interface which limits the open-circuit voltage (V_{OC}) of the complete cell to ~1.12 V. Inserting ultrathin interlayers between the perovskite and transport layers allows substantial reduction of these interfacial losses at both the *p* and *n* contacts. Using this knowledge and approach, we demonstrate reproducible dopant-free 1 cm^2 PSCs surpassing 20% efficiency (19.83% certified) with stabilized power output, a high V_{OC} (1.17 V) and record fill factor (> 81%).

Introduction

The solution processability and potential for simple manufacturing from earth abundant materials drives research efforts into perovskite solar cells in the search for cheap, printable photovoltaic devices. The discovery that perovskites effectively sensitize titanium dioxide (TiO_2) in dye-sensitized solar cells in 2009,[1] and the demonstration of the first thin-film solid-state perovskite solar cells in 2012[2,3] spurred tremendous research efforts concerning the understanding and optimization of perovskite-based optoelectronic devices. While power conversion efficiencies (PCE) of perovskite solar cells[4] are rapidly approaching industrially engineered silicon and inorganic thin film solar cells,[5] several key issues remain that need to be overcome. These include fundamental questions regarding recombination losses,[6] long term stability[7] and difficulties in scaling to large electrode areas.[8] Today it is well known that in order to unlock the full thermodynamic potential of perovskite solar cells it is imperative to suppress all non-radiative recombination losses which manifest as increased dark currents and ideality factors larger than one, limiting both the cells' open-circuit voltage (V_{OC}) and the fill factor (FF).[6,9] One of the most challenging tasks in this regard is being able to pinpoint the origin of these losses in a complete device under operational conditions. In general, recombination losses may either occur in the perovskite bulk[4,6,10] or close to the interface of an adjacent transport layer as a result of a higher density of trap states at the surface.[11,12] Likewise, recombination may also occur across interfaces[13–15] between charges in the transport layer and minority carriers in the perovskite, or in the transport layers themselves.[15] The situation becomes more challenging for comparatively large area cells (e.g. 1cm^2) where additional losses come from inhomogeneities of the active perovskite absorber but also at the interfaces to the transport layers, while also transport resistances become an issue.[8] Knowing the origin of the non-radiative recombination losses would greatly facilitate targeted improvements in device performance.[13] This is particularly relevant for planar perovskite devices in *pin*-configuration which still lag behind the most efficient *nip* cells[4,16–20] due to their lower open-circuit voltage and higher non-radiative recombination losses (e.g. 1.15 V for record *pin*-cells[16] compared to > 1.23 V for *nip*-cells[13,18]). Nevertheless, *pin*-type cells are very attractive for single junctions solar cells as they require only ultrathin undoped charge transport layers (e.g. 8 nm PTAA, 30 nm C_{60})[9] without the need for extensive chemical doping[9] and annealing at temperatures above 100 °C. This renders their fabrication compatible with roll-to-roll deposition on flexible plastic substrates. Moreover, a *pin* perovskite device architecture is required for Si/perovskite tandem applications in combination with well-established solar cell technologies based on *p*-type silicon.[21,22] Thus, a detailed investigation of non-radiative recombination losses and which interface represents the bottleneck for cell efficiency is urgently needed.

In this paper we use a combination of steady-state and transient photoluminescence (PL and TRPL) measurements to pinpoint the origin of non-radiative recombination losses in devices. In particular, we determine the recombination kinetics and quasi-Fermi level splitting (QFLS) in sample stacks consisting of the perovskite absorber-only, and perovskite/charge transport layer heterojunctions on length scales

relevant to our solar cells (1 cm^2). We identify the main limitation to higher performance to be minority carrier recombination at the heterojunction with the organic CTLs. The latter losses are found to be surprisingly similar at the electron- and hole-selective interfaces. These findings guided us to optimize the hole-selective interface through the use of a conjugated polyelectrolyte which almost entirely supressed interfacial recombination while simultaneously improving the wetting of the perovskite solution on the HTL surface delivering reproducible 1cm^2 sized devices. With the knowledge that the V_{OC} of the final device is now largely defined by the QFLS of the inferior perovskite/C60 heterojunction we introduced an ultrathin layer of LiF (6 Å to 1 nm) between the absorber and the ETL. This allowed us to reduce the interfacial recombination loss at the electron-selective interface by 35 meV. Supressing the non-radiative recombination at both interfaces directly resulted in critical V_{OC} and FF improvements in complete devices allowing 1 cm^2-size cells with ~20% efficiency and stabilized maximum power output and high reproducibility. This is currently the highest certified efficiency for a published 1 cm^2 perovskite solar cell structure. Lastly, numerical simulations highlight the importance of interface optimizations in relation to bulk optimizations for further developments.

Devices architecture

Our work builds on recent advancements on the understanding and improvement of *pin* devices.[11,20,23] The chemical structures of PTAA, perovskite and C_{60} as used in our standard cells with architecture [(ITO (150 nm)/PTAA (8 nm)/perovskite (400-500 nm)/C_{60} (30 nm)/BCP (8 nm)/Cu (100 nm)] are shown in **Figure 1a**: For the active layer material, we chose the previously reported "triple cation perovskite" mixture with the composition $CsPbI_{0.05}[(FAPbI_3)_{0.89}(MAPbBr_3)_{0.11}]_{0.95}$ as it delivers amongst the best photovoltaic performance. We note that while we focus on triple cation cells we have also generalized the results to $MAPbI_3$ and $(Cs_{0.05}FA_{0.95})PbI_3$ absorber layers as discussed at the end of the manuscript. **Figure 1b** displays a schematic energy level diagram based on the results from ultraviolet and inverse photoemission spectroscopy,[15] and proposes possible recombination mechanism.

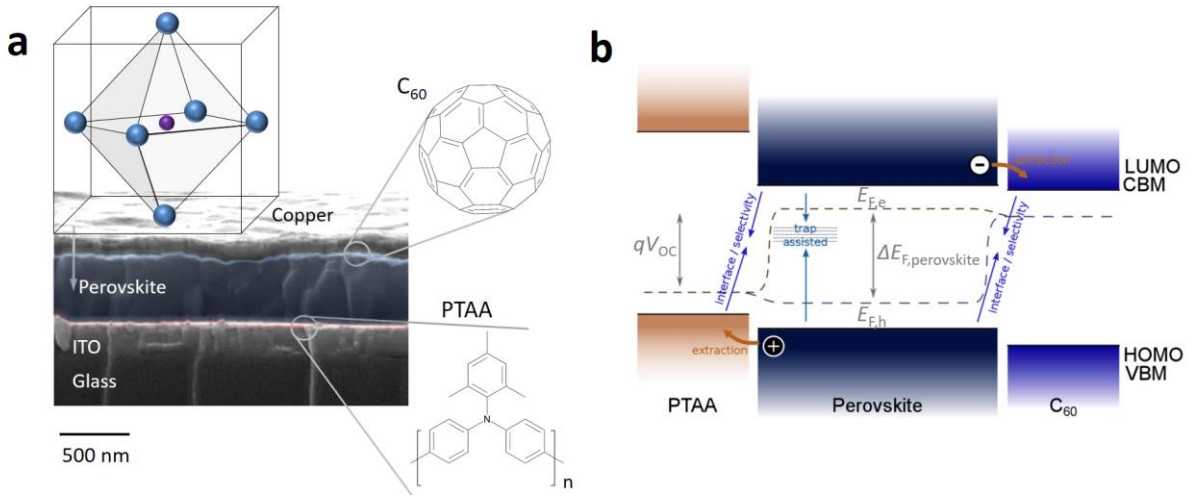

Figure 1. Schematic device architecture and energetics. (a) *Cross-section of a full device comprising from bottom to top: the glass and transparent conducting electrode (ITO), a hole-selective polymeric*

layer of PTAA, the perovskite absorber layer, the electron selective C_{60} layer and the metallic top electrode (copper). Chemical structures are shown for PTAA and C_{60}, and a schematic perovskite crystal structure. The scales bar represents 500 nm. ***(b)*** *Schematic energy level diagram and pathways of non-radiative recombination via traps in the perovskite bulk or at the interfaces as a minority carrier loss. Also shown is the extraction of majority carriers to the transport layers, the quasi-Fermi levels of electrons ($E_{F,e}$) and holes ($E_{F,h}$) and the resulting quasi-Fermi-level splitting ($\Delta E_{F,perovskite}$) and the recombination-limited open-circuit voltage (V_{OC}).*

One of the most important considerations for scaling the device area is the electrode architecture due to the relatively high sheet resistance of the transparent conductive electrode (TCE).[8] It is thus essential to minimize the length carriers have to traverse through the comparably high resistance electrode (that is ITO versus copper). **Figure 2a** shows the current-voltage characteristics of optimized 1cm^2 cells with electrode width of 8 mm and 4 mm, which demonstrates that the FF can be increased from 69% to 77.9% by simply reducing the width of the active area. This is also in agreement with numerical solutions of the Shockley equation for different electrode aspect ratios as illustrated in **Figure 2b** which confirm a roughly 2% absolute efficiency gain through the FF (**Supplementary Figure 1**). This approach is in principle scalable, as the rectangular cells can be connected using laser patterning[24] while the electrode width may be slightly increased using a lower resistance ITO substrate (e.g. 10 Ω/sqr).

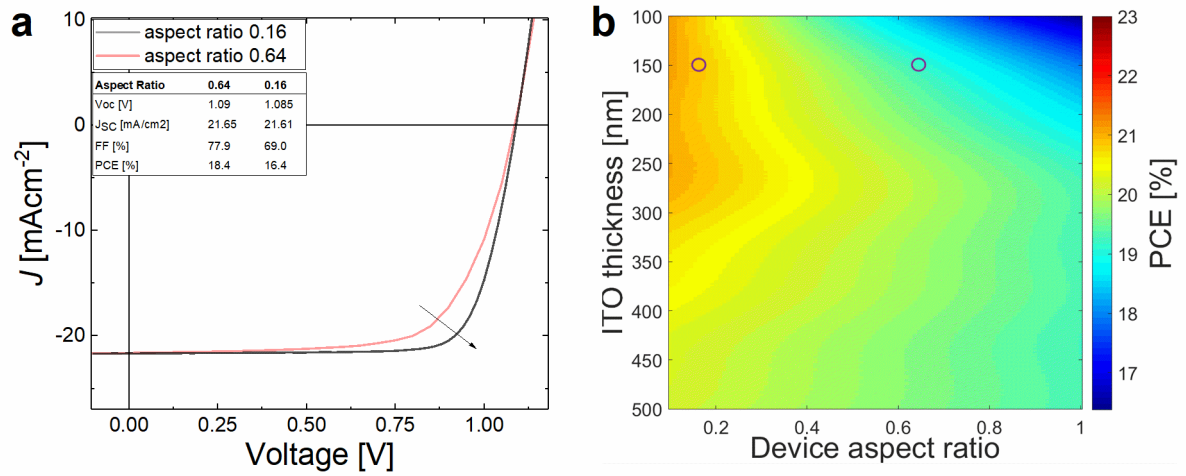

Figure 2. ***Optimization of electrode design.*** ***(a)*** *Experimental JV-curves of 1 cm^2 cells comprising a PTAA/perovskite/C_{60} stack with different electrode aspect ratios. Reducing the active area width from 8 mm (aspect ratio 0.64) to 4 mm (aspect ratio 0.16) while keeping the active area the same improved the FF by approximately 9% as indicated by the arrow.* ***(b)*** *Simulated solar cell efficiencies using optical simulations of the obtainable short-circuit current and subsequently the Shockley equation with a finite ITO series resistance depending on its thickness and the device aspect ratio. An internal cell resistance of 1.5 Ωcm^2 (for a 1 cm^2-size cell) and an ideality factor of ~1.5 were assumed as previously determined.*[6] *The two circled points correspond to the two devices from panel* ***(a)****.*

Non-radiative Recombination Losses

Among the most widely used and trusted techniques in the community to study the fate of photogenerated charges in perovskite solar cells is time resolved photoluminescence (TRPL).[25,26] At sufficiently low fluences a mono-exponential decay is usually observed, indicative of an underlying non-radiative trap-induced recombination that gradually reduces the density of emitting species and hence the PL signal.[6,10,27] The fluence dependence of the TRPL signals is shown in **Supplementary Figure 2**. **Figure 3** shows the result of such an experiment on a neat perovskite film, which displays a long PL lifetime of approximately half a microsecond, comparable to previously reported perovskite films on TiO_2.[17] Considerably longer lifetimes have been reported in exceptional cases; for example, a lifetime of 8 µs was recently realized through surface passivation of the perovskite with tri-*n*-octylphosphine (TOPO).[27] As recently demonstrated,[6] the achievable V_{OC} in case of dominant Shockley-Read-Hall recombination can be predicted from the carrier lifetime (τ_{SRH}). As we detail in **Supplementary Note**, a SRH lifetime of 500 ns as deduced from the exponential PL decay of the neat perovskite layer should limit the open-circuit voltage to approximately 1.215 V at room temperature. Given that the measured V_{OC} of the device is significantly lower suggests that addition of the CTLs induces substantial non-radiative recombination losses.

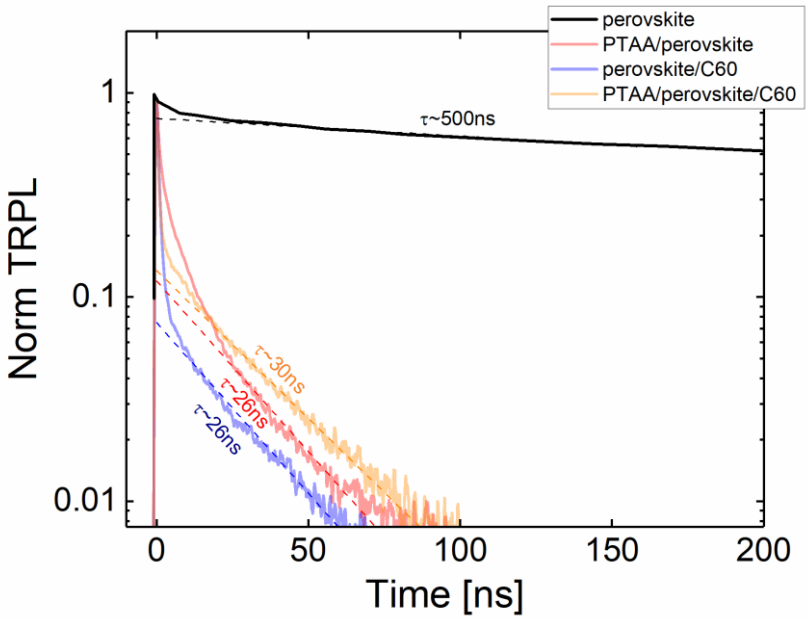

Figure 3. Impact of transport layers on kinetics of radiative recombination. *Mono-exponential transient photoluminescence (TRPL) decay of a neat perovskite film indicating the dominance of trap-assisted recombination in the bulk or the surface. The corresponding mono-exponential lifetime is around 500 ns potentially allowing a Voc of 1.215V (see* ***Supplementary Note****) if no additional interface recombination losses were present. The TRPL signals of perovskite/transport layer heterojunctions show a bi-exponential decay indicating rapid charge extraction and interfacial recombination on different timescales. The films were illuminated at 470 nm (~30 nJcm^{-2}) through the organic layer, and C_{60} in case of the pin-stack.*

Figure 3 demonstrates the large impact of the addition of charge transporting layers on the TRPL decay, which is consistent with other previously reported studies.[17] Notably, large reductions in PL lifetimes are seen independent of whether the PTAA is added between the glass and the active material or coated on top of the perovskite film (on glass), indicating that differences in perovskite morphology related to the nature of the underlying substrate are of minor importance in determining the PL lifetime (see **Supplementary Figure 3**). Interestingly, all samples comprising one or two transport layers exhibited a similar and fast bi-exponential decay. As pointed out previously,[6,28] this may be either due to the rapid extraction of charges on (sub) ns timescales (quenching), or increased non-radiative recombination losses – two processes that are inherently difficult to disentangle from the TRPL signal alone. However, unless one transport layer completely depletes the perovskite bulk of one carrier type, the impact of non-radiative interface recombination will be visible in the signal given a high enough signal-to-noise ratio of the measurement. As the bulk recombination happens at rather long timescales (lifetime ~ 500 ns), it can be concluded that the TRPL signals on the films with the transport layers present are subjected to additional non-radiative interface recombination. Following this line of argument, we attribute the fast initial decay to the loss of carriers at the interfaces due to charge extraction to the transport layers and/or to interface recombination, and the second decay (for which the mono-exponential lifetimes are provided in **Figure 3**) to interface recombination. In accordance with this, the initial decay becomes less pronounced and smeared out when increasing the excitation wavelength, i.e. when light penetrates deeper into the perovskite layer (see **Supplementary Figure 2**). The rather similar decays after the initial drop in the samples with either PTAA or C_{60} indicate that the two perovskite/organic heterojunctions are equally limiting the V_{OC} due to additional non-radiative recombination losses at the interfaces. After carriers reach a quasi-equilibrium distribution, the lifetime (τ_{II}) can be described by an equilibrium between the bulk decay (τ_{Bulk}), diffusion time to the surface $\left(\frac{4d^2}{\pi^2 D}\right)$, and interface loss velocity $\left(\frac{d}{S_1}\right)$, i.e. $\frac{1}{\tau_{II}} = \frac{1}{\tau_{Bulk}} + \left(\frac{4d^2}{\pi^2 D} + \frac{d}{S_1}\right)^{-1}$.[25,28] Using the bulk lifetime of 500-785 ns, a mobility of 30 $cm^2V^{-1}s^{-1}$,[29] d = 400 nm, and the measured τ_{II} value of 20-30 ns would result in an interface loss velocity of S_1 ~ 1.6x10^3 – 2.1x10^3 cm/s at the interface between the charge transport layer and the perovskite. However, other processes may potentially influence the TRPL signal as well, such as a decelerating charge extraction, light soaking effects,[30] photon-recycling,[25,26] or a graded generation profile. Thus, it is clear that whilst TRPL is a useful guide to recombination losses, it by no means provides definitive mechanistic insight.

Photoluminescence and Quasi-Fermi Level Splitting

A much more direct way to quantify the additional non-radiative recombination losses at the perovskite/organic interfaces is steady-state PL as the absolute PL intensity (I_{PL}) is a direct measure of the quasi-Fermi level splitting (QFLS or ΔE_{F}).[31–36] Here, we use hyperspectral absolute photoluminescence imaging to create depth averaged maps of the QFLS on the neat perovskite films in

comparison to multilayer samples comprising one or both types of transport layers. This approach has been recently used by El-Hajje et al.[32] to spatially resolve the opto-electronic quality of evaporated methylammonium lead iodide junctions, and to study the hole blocking of different ETLs. Moreover, absolute PL has been recently applied to disentangle interfacial and bulk recombination losses in *nip*-cells by Sarritzu et al.,[34] although the QFLS was not compared to the device voltage and thus open-circuit voltage losses not directly quantified. As recently discussed,[33] there are different approaches to calculate ΔE_F from absolute PL spectra, which are all based on Würfel's generalized Planck law[31] that describes the non-thermal radiation of a semiconductor:

$$I_{PL}(E) = \frac{2\pi E^2 a(E)}{h^3 c^2} \frac{1}{\exp\left(\frac{E - \Delta E_F}{kT} - 1\right)} \quad \text{(eq. 1)}$$

Here, $a(E)$ is the photon energy (E) dependent absorptivity, c is the speed of light, h is the Planck constant. Under the assumption that for emission energies above the PL maximum, $a(E)$ approaches 1, **equation 1** can be simplified to

$$\ln\left(\frac{I_{PL}(E) h^3 c^2}{2\pi E^2}\right) = -\frac{E}{kT} + \frac{\Delta E_F}{kT} \quad \text{(eq. 2)}$$

Equation 2 allows to deduce ΔE_F simply from fitting the high energy slope of the PL emission.[37] By applying **equation 2** to every spectrum associated with each pixel (10 µm in diameter) of the hyperspectral images, ΔE_F distribution maps can be created. **Figure 4** shows the depth averaged QFLS maps (1 cm^2) of the neat triple cation perovskite film, with either the PTAA or C_{60} or both transport layers being present. The perovskite absorber exhibits a homogenous profile with a QFLS of approximately 1.21 eV (we note a 20 meV global systematic error on all maps). While this value is remarkably close to the V_{OC} obtained from the TRPL lifetime according to **Supplementary Note 1**, it is substantially below the radiative V_{OC} of approximately 1.345 eV. The latter was estimated from the dark generation current $J_{0,rad}$ ~ 4x10^{-21} A/cm^2 (see **Supplementary Figure 4**). This approach for calculating the radiative V_{OC} limit has been extensively applied to perovskite solar cells as shown in refs.[38–40] and dates back to Shockley-Queisser ref.[41] We also note that the emitted PL can be affected by photon-recycling.[25,26] However, this does not affect our conclusions, because it is the external PL quantum yield (PLQY) that determines the QFLS and maximum achievable device V_{OC}.[42] **Figure 4** also shows that the QFLS of the perovskite/C_{60} film is significantly reduced to approximately ~1.136 eV ± 10 mV, while the PTAA/perovskite film exhibits a QFLS of ~1.125 eV ± 10 mV. It is important to note that, compared to the neat absorber material with a PLQY of ~0.5 %, addition of PTAA or C_{60} results in a large reduction of average photoluminescence efficiency (e.g. 0.017% for a perovskite/C_{60} film) which also means a large increase in the non-radiative loss current (~30x in case of perovskite/C_{60} compared to the neat

absorber material). Yet, despite the different nature of these two interfaces, the non-radiative recombination losses at both interfaces are surprisingly similar (lowering the QFLS by ~80 meV compared to the neat absorber), which is consistent with the TRPL results. For the (unoptimized) *pin* stack (glass/PTAA/perovskite/C_{60}) we obtain a ΔE_F of approximately 1.121V ± 10 mV which perfectly matches the average V_{OC} in complete cells under comparable illumination intensities (see below). Interestingly, this value lies only slightly below the QFLS of samples with only one transport layer present, indicating that the non-radiative recombination losses at each individual interface are both reducing the $I_{PL}(E)$, yet the QFLS only through the logarithm in **Equation 2**. We also note a good reproducibility and homogeneity of the QFLS on the neat perovskite film and all films with C_{60}, except for the glass/PTAA/perovskite heterojunctions for which we observed a relatively large batch-to-batch variation (with the average QFLS ranging from 1.09 eV to 1.16 eV, see **Supplementary Table 1**). On the other hand, no difference in the QFLS was observed between a PTAA/perovskite film on a glass or an ITO substrate which suggests no additional non-radiative recombination losses at the ITO/PTAA interface (see **Supplementary Figure 5**).

Although **Figure 4** shows that the perovskite absorber imposes a large limitation on the V_{OC}, we would expect that it is the weakest component of the (*pin*) stack that dominates the non-radiative loss current and sets the upper limit for the device V_{OC} (in our case both interfaces equally). In order to further clarify the importance of interfacial optimizations in relation to bulk optimizations depending on the selectivity of the interlayers, we numerically simulated the open-circuit voltage of a *pin* device stack by varying the interface recombination velocities and the bulk lifetime using a drift-diffusion simulator (**Supplementary Figure 6)**.[43] Applying the measured interface-recombination velocity in our structures prior to optimization (i.e. ~2000 cm/s) and bulk lifetime (500 ns) as input parameters, the simulation accurately describes the V_{OC} of our standard cells. The simulations clearly show that even if we improved the perovskite bulk lifetime multiple times (>>500 ns), no V_{OC} improvements are possible when the interface recombination velocities stay at 2000 cm/s. Thus, we conclude that the V_{OC} of our cells is entirely limited by the interfaces, and any improvement of the bulk would be lost due to rapid interfacial recombination. Thus, it is essential to systematically improve the interfaces as we discuss in the following.

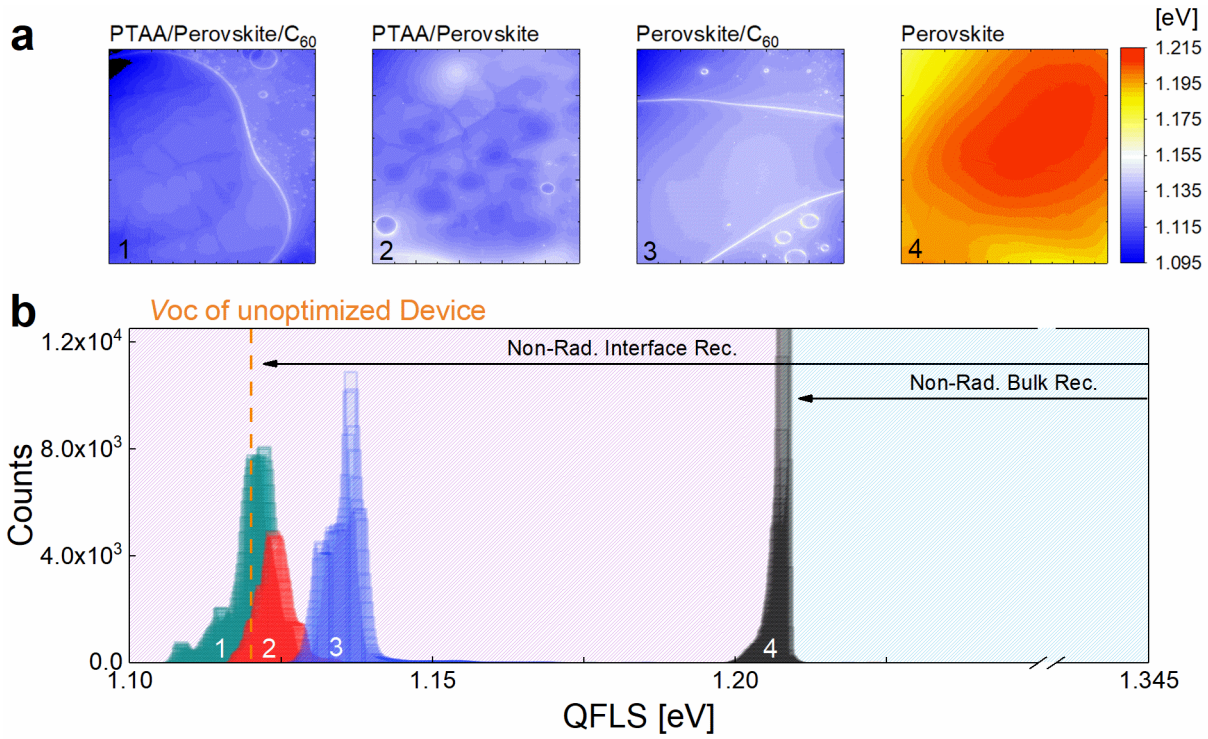

Figure 4. Visualization of non-radiative interfacial recombination through absolute photoluminescence imaging. ***(a)*** *Quasi-Fermi level splitting maps (1 cm^2) and* ***(b)*** *corresponding energy histograms on perovskite-only, perovskite/C_{60}, PTAA/perovskite, and PTAA/perovskite/C_{60} films on glass. The neat perovskite absorber allows a QFLS (and thus potential V_{OC}) of approximately 1.208 eV (at 300 K) which is consistent with the transient photoluminescence decay (**Figure 3**) but significantly below the QFLS in the radiative limit (1.345 eV) as indicated by the arrow. Addition of only one transport layer (either PTAA or C_{60}) induces additional non-radiative recombination pathways, which lower the QFLS down to approximately 1.125-1.135 eV. The pin-junction with both transport layers adjacent to the perovskite absorber still has an average QFLS of approximately 1.121 eV. The arrow shows that interfacial recombination dominates the non-radiative recombination losses in the stack. The films were excited at 450 nm with a 1 sun equivalent intensity and the histograms were recorded on 5 mm x 5 mm squares in the middle of the films without edge effects (PL quenching) due to the encapsulation glue as visible in sample 1 and 3 and 4.*

Suppression of Interfacial Recombination

Following the approach proposed by Lee et al.[44] to improve the wettability of hydrophobic CTLs**,** we functionalized the PTAA layer with the interface compatibilizer PFN-P2 - a conjugated polyelectrolyte (CPE). In line with their findings,[44] the amphiphilic properties of PFN-P2 improved the wetting of the perovskite film on the hydrophobic PTAA, thus greatly enhancing the fabrication yield of our cells without frequent pinhole formation. In order to reveal possible changes of the layers morphology as a function of the underlying substrate, we performed top and cross section scanning electron microscopy (SEM) measurements of perovskite films deposited on glass, glass/ITO/PTAA, and

glass/ITO/PTAA/PFN. The images shown in **Supplementary Figure 7** demonstrate perovskite grains ranging from tens of nanometres to micrometres and indicate, at least qualitatively, small changes of the perovskite bulk morphology across these substrates. Importantly, we find that PFN-P2 causes a substantial reduction of the recombination at the HTL contact as shown in **Figure 5a, b.** This resulted in an average QFLS value very close to the value for the neat perovskite (~1.21 eV) while simultaneously improving the homogeneity of the absolute PL image. In order to check whether PFN-P2 itself passivates the perovskite surface by reducing trap assisted recombination independent of the presence of the HTL/perovskite interface, we compared QFLS maps of glass/perovskite and glass/PFN-P2/perovskite samples (**Supplementary Table 1**). No differences in the QFLS were found, which allows us to assign the increased QFLS of the HTL/PFN-P2/perovskite junction to supressed interfacial recombination. In accordance to this, we recorded a significantly slower TRPL decay on samples including PFN-P2 (**Figure 5c**). Motivated by this success, we aimed to reduce the detrimental recombination at the perovskite/ETL interface. Different strategies have been reported to block holes at the *n*-interface, such as polystyrene[45] or choline chloride[16] for *pin*-cells or Ga2O3 for *nip*-cells.[13] However, for our triple cation *pin*-perovskite solar cells we found the most significant effect on the QFLS and device efficiency when inserting an ultrathin layer (0.6 nm – 1 nm) of LiF between the perovskite and C_{60}, causing a reduction of the non-radiative interfacial recombination loss by 35 meV (**Figure 5d, e**). Again, as shown in **Figure 5f**, the increase in QFLS was correlated with a slower mono-exponential TRPL decay (with a lifetime that increased from 26 ns to 180 ns for a perovskite/C_{60} and perovskite/LiF/C_{60} film on glass, respectively.)

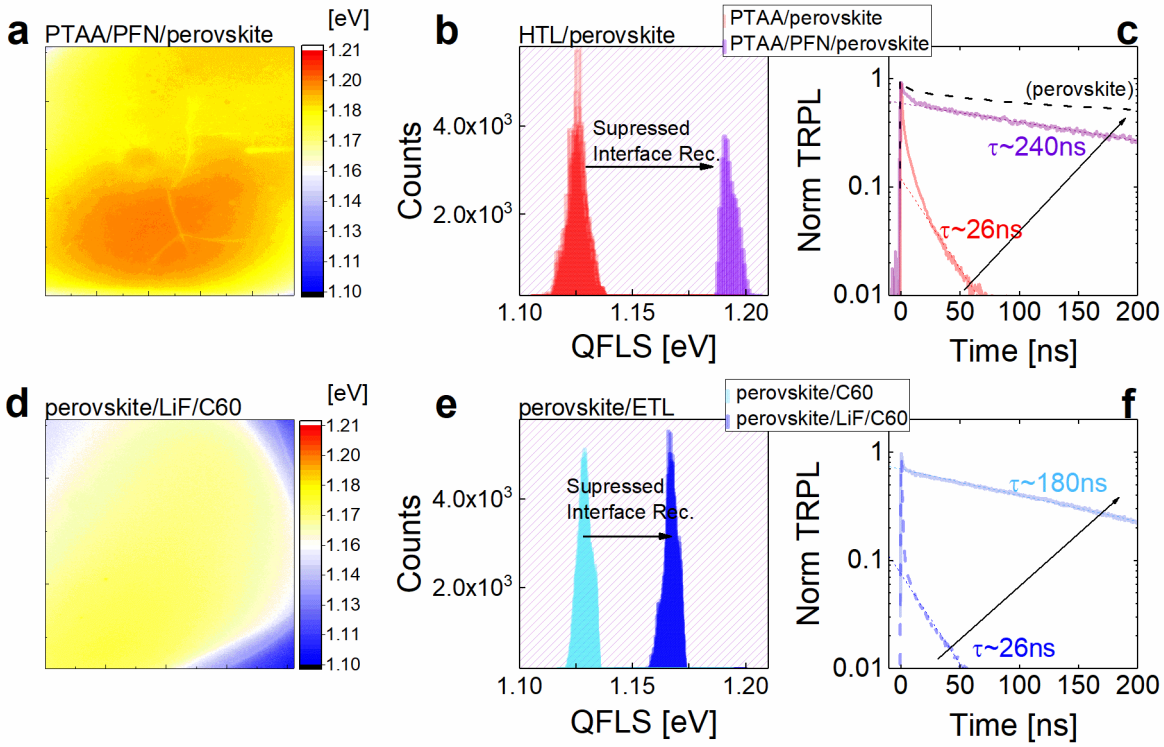

Figure 5. Suppression of interfacial recombination through interlayers. (a) *Quasi-Fermi level*

splitting (QFLS) map (1x1 cm) and ***(b)*** *QFLS histogram of a PTAA/PFN-P2/perovskite film on glass demonstrating a comparatively high average QFLS of approximately 1.19 eV. This represents a significant enhancement of approximately 65 meV compared to the QFLS of the PTAA/perovskite film and approaches the QFLS potential of the neat perovskite by 20 mV.* ***(d)*** *QFLS map (1x1 cm^2) and* ***(e)*** *QFLS histogram of a perovskite/LiF/C_{60} film on glass demonstrating the reduced interfacial recombination loss at the n-contact. Importantly, the average QFLS of the perovskite/LiF/C_{60} stack (1.169 eV) is again almost identical to the Voc of our optimized cells (1.16 – 1.17V). The histograms were recorded on a 5mm x 5mm square in the middle of the films without edge effects (PL quenching) due to the encapsulation glue.* ***(c, f)*** *TRPL transients highlighting the significant prolongation of the carrier lifetime when either PFN-P2 or LiF is added as an interlayer.*

Photovoltaic performance

Introducing both interlayers led to considerable improvements of the cell efficiency (from average 18% to 20%) through an increase in V_{OC} and FF (see **Supplementary Figure 8** for the performance of 6 mm^2 sized devices). Importantly, the average V_{OC} of cells with both interlayers present is 1.16 V which compares well with the average QFLS of the perovskite/LiF/C_{60} stack and the complete device stack (~1.17 eV, see **Supplementary Table 1**). Measuring the V_{OC} as a function of light intensity on cells with and without both interlayers reveals a similar ideality factor but a smaller dark recombination current density (J_0) for the interlayer-containing device, indicating that these additional layers do affect the rate but not the overall nature of the recombination process (**Supplementary Figure 9)**. From the device manufacturing perspective, introducing PFN-P2 greatly improved the homogeneity of the perovskite films allowing us to manufacture 1cm^2 cells without the frequent pinhole formation as encountered in our standard cells (without the interlayers) resulting in reproducible high efficiencies. Typically, without PFN-P2, only one out of three 1cm^2 cells resulted in efficiencies above 18%, while this PCE could be safely achieved for more than 90% of cells if PFN-P2 was included. Cells with PFN-P2 (but without LiF) reached efficiencies up to 19.6% (J_{SC} = 21.85 mAcm^{-2}, V_{OC} = 1.143 V, FF = 78.6% **Supplementary Figure 10**) when measured with an aperture mask (1.018 cm^2) at 25°C. The short-circuit current matched the integrated EQE and solar spectrum product (21.5 mAcm^{-2}) within an error of less than 2% (**Supplementary Figure 11**). This cell was certified by an independent accredited institute (Institute for Solar Energy, Fraunhofer Freiburg), which gave a stabilized PCE of 19.22% **Supplementary Figure 12**) with a negligible mismatch to our *JV*-measurement in terms of current. Moreover, encapsulated cells were stable over at least 100 hours under MPP (maximum power point) tracking conditions in air and constant illumination from a white LED with 1 sun equivalent light intensity, with only a small loss in efficiency (0.6% absolute) (**Supplementary Figure 13**). We also note that using 10 Ω/sqr ITO substrates instead of our standard 15 Ω/sqr ITO substrates allowed us to achieve FFs above 81% which is, to our knowledge, 3% higher than the highest reported FFs for 1 cm^2 size cells (**Supplementary Figure 14**).[46] As expected from the QFLS analysis, the V_{OC} of cells is

significantly increased through introduction of the LiF interlayer (~ 1.17 V), pushing the PCE of our 1 cm^2 cells up to a value of 20.0% with virtually no hysteresis and stable power output as shown in **Figure 6**.

However, compared to the highest certified $1cm^2$ cells with a PCE of 20.9%[47] (J_{SC} of 24.9 $mAcm^{-2}$, geometry and structure currently unpublished) a remaining limitation of our cells is their relatively low short-circuit current. Thus, in order to lower the bandgap of the perovskite layer, we optimized the ratio of $FAPbI_3$ to $MAPbBr_3$. We found that using a ratio of 89:11 allows a significant improvement in short-circuit current (0.5-1 $mAcm^{-2}$) with surprisingly minimal loss in V_{OC} and efficiencies up to 21.6% for small 6 mm^2-size cells (J_{SC} = 23.2 $mAcm^{-2}$, V_{OC} = 1.156V, FF = 80.4%) (**Supplementary Figure 8**). As for the 1 cm^2 devices, **Supplementary Figure 15a** shows our present hero device with both interlayers included (PFN-P2 and LiF) fabricated from a $CsPbI_{0.05}[(FAPbI_3)_{0.89}(MAPbBr_3)_{0.11}]_{0.95}$ perovskite with an efficiency of 20.3%, notably again with very small mismatch versus the integrated EQE-solar spectrum product (**Supplementary Figure 15b**). This cell was certified by Fraunhofer-ISE resulting in a PCE of 19.83% which is currently the highest certified efficiency of a $1cm^2$ size perovskite cell with published geometry and structure (**Supplementary Figure 16** and **17**).[4] We also highlight the important fact that the efficiency of our cells is stabilized in contrast to most previous perovskite solar cells certifications which are denoted as "not stabilized".[4,47]

Lastly, we note that our concept to identify and suppress interfacial recombination can be successfully generalized to other perovskite compositions including the standard methylammonium lead iodide absorber (MAPI) where we reached efficiencies slightly above 20%; as well as Cs containing formamidinium lead iodide perovskite cells $(Cs_{0.05}FA_{0.95})PbI_3$ with close to 20% PCE (**Supplementary Figure 18**). The latter system is particularly interesting as pure $FA_{0.95}PbI_3$ exhibits a bandgap of 1.47 eV which is closer to the optimum bandgap in the Shockley-Queisser model.[48] However, reports of pure $FAPbI_3$ cells are rare and the efficiencies of such devices lag significantly behind the mixed perovskite systems.[48–50] Application of absolute PL on the individual perovskite/charge transport layer junctions proves once again substantial reduction of interfacial recombination by the addition PFN and LiF at the *p* an *n*-contact, respectively (**Supplementary Table 2**). Notably, this allowed the devices to reach record efficiencies for MA/Br-free $FAPbI_3$ perovskite solar cells which further underlines the potential of our recombination analysis and interfacial engineering approach.

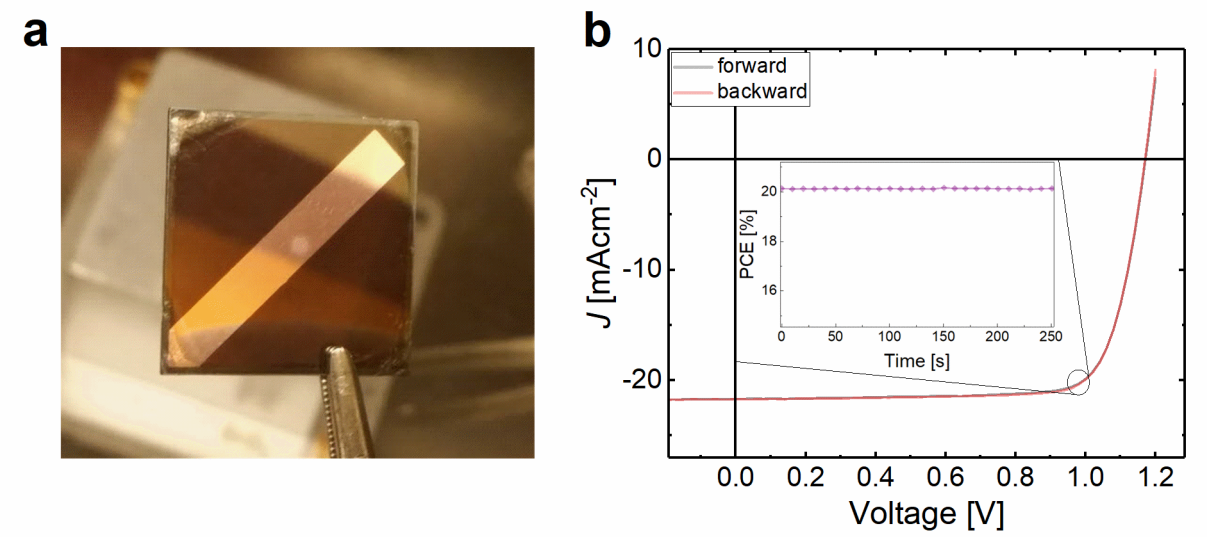

Figure 6. 20% efficient pin-type perovskite cells with 1 cm² active area (a) *Photograph of a fabricated 1cm² cell with rectangular active electrode area.* ***(b)*** *1cm² perovskite cells reaching 20% PCE were achieved using a combination of PFN-P2 and LiF interlayers (J_{SC} = 21.7 mA/cm², FF=78.6%, V_{OC} = 1.17 V) as measured with aperture mask (1.018 cm²) at 25°C. The inset shows the stabilized power output at 20.1%.*

Conclusions

In conclusion, hyperspectral photoluminescence imaging allowed us to identify the origin of non-radiative recombination loss channels through mapping of the QFLS of the relevant perovskite/transport layer combinations. We found significant non-radiative recombination losses in the neat perovskite layer which reduce the potential V_{OC} by approximately 135 mV compared to the radiative limit of this type of perovskite (1.345 V). However, interface recombination at each individual hybrid interface (PTAA/perovskite and perovskite/C_{60}) dominates the non-radiative loss current in the stack and results in a significant further reduction of the QFLS down to ~1.13 eV. In line with this interpretation, we achieved a considerable improvement of the device performance by applying PFN-P2 and LiF as interfacial layers, which supressed the recombination losses by 65 meV and 35 meV at the *p*-and-*n*-interface, respectively. The reduced recombination and increased QFLS splitting resulted in significant V_{OC} and FF gains, which in combination with an optimized composition of the perovskite layer led to a PCE above 20% for 1 cm² sized cells with a certified PCE of 19.83% and stabilized power output. This work demonstrates how interfacial recombination losses can be unambiguously identified and supressed, and paves the way to reach the thermodynamic limit for perovskite solar cells through further minimization of interface and trap-assisted recombination in the absorber layer.

Methods

Hyperspectral Absolute Photoluminescence Imaging: Excitation for the PL imaging measurements was performed with two 450 nm LEDs equipped with diffuser lenses. The intensity of the LEDs was adjusted to ~1 sun by illuminating a contacted perovskite solar cell (short circuit) and matching the current density to the short circuit current measured in the JV sun simulator (The measured short circuit current density of the solar cell under this illumination was 22.2 mA/cm^2. The photoluminescence image detection was performed with a CCD camera (Allied Vision) coupled with a liquid crystal tuneable filter. The system was calibrated to absolute photon numbers in two steps in a similar way to the process described by Delemare et al.[51] For this purpose an IR laser diode and a spectrally calibrated halogen lamp was coupled to an integrating sphere. The pixel resolution of the images corresponds to about 10 μm in diameter. Sets of images from 650 nm to 1100 nm with 5 nm step size were recorded. All absolute PL measurements were performed on films with the same thicknesses as used in the operational solar cells.

Time Resolved PL: PL data was acquired with a TCSPC system (Berger & Lahr) after excitation with a pulse-picked and frequency-doubled output from a mode-locked Ti:sapphire oscillator (Coherent Chameleon) with nominal pulse durations ~100 fs and fluence of ~ 30 nJ/cm² at a wavelength of 470 nm. The samples were excited from the side of the interface we sought to investigate (i.e., glass side for PTAA and top side for the other samples). The short wavelength excitation was chosen to specifically excite the samples close to the interface we were interested in. SEM images were acquired with a Zeiss Ultra Plus SEM. All TRPL measurements were performed on films with the same thicknesses as used in the operational solar cells. A global systematic error of 20 meV (or equivalently a factor of ~2 in PL efficiency) was estimated based on uncertainties in the optimum approach to calculate the QFLS (Equation 2), as well as small uncertainties in the estimation of the bandgap and the temperature.

Device Fabrication: Pre-patterned 2.5x2.5cm² 15 Ω/sq. ITO substrates (Automatic Research, Germany) were cleaned with acetone, 3% Hellmanex solution, DI-water and *iso*-propanol, by sonication for 10min in each solution. After a microwave plasma treatment (3min., 200W), the samples were transferred to a N_2-filled glovebox. A thin (~8 nm) PTAA (Sigma-Aldrich) layer was spin coated from a 1.5mg/mL toluene solution at 6000 rpm for 30 seconds. The layers were subsequently annealed inside a nitrogen filled glovebox (< 1 ppm H_2O and O_2) at 100 °C for 10 min. After the substrate was allowed to cool for 5 min, a 60 μL solution of PFN-P2 (0.5 mg/mL in methanol) was added onto the spinning substrate at 5000 rpm for 20 s resulting in a film with thickness below the detection limit of our AFM (< 5nm). The perovskite layer was prepared using an anti-solvent treatment. We found an improvement in V_{OC} and reproducibility by switching the anti-solvent from DEE to ethyl acetate (EA), which is miscible with DMF:DMSO mixtures and has a higher boiling point (77.1°C) and an optimal polarity of approximately 4.5. Therefore, all cells reported here were fabricated using EA as the anti-solvent. Then, the perovskite layer was deposited by spin-coating at 4000 rpm for 35 seconds. 10 Seconds after the

start of the spinning process, the spinning substrate was washed with 300 µL EA for approximately 1 second (the anti-solvent was placed in the centre of the film). The perovskite film was then annealed at 100 °C for 1 hr on a preheated hotplate. The samples were transferred to an evaporation chamber and LiF (6 Å to 1 nm), C_{60} (30 nm), BCP (8 nm) and copper (100 nm) were deposited under vacuum (p = 10^{-7} mbar). After completion, the glass side of the 1cm^2-size cells was coated with a Brisbane Materials Technology (Australia Pty Ltd) anti-reflection coating optimised for a broad band spectral response in the AM1.5 window.

Current density-voltage characteristics: JV -curves were obtained in a 2-wire source-sense configuration with a Keithley 2400. An Oriel class AAA Xenon lamp-based sun simulator was used for illumination providing approximately 100 mW cm^{-2} of AM1.5G irradiation and the intensity was monitored simultaneously with a Si photodiode. The exact illumination intensity was used for efficiency calculations, and the simulator was calibrated with a KG5 filtered silicon solar cell (certified by Fraunhofer ISE). A spectral mismatch calculation was performed based on the spectral irradiance of the solar simulator, the EQE of the reference silicon solar cell and 3 typical EQEs of our cells. This resulted in 3 mismatch factors of M = 0.9949, 0.9996 and 0.9976. Given the very small deviation from unity the measured J_{SC} was not corrected by the factor $1/M$. All EQEs resented in this work were measured by ISE-Fraunhofer.

Coupled Optical and Shockley-Queisser-Modelling: We employed an optical modelling tool[52] to calculate the photogenerated current inside the perovskite material depending on the thickness of the ITO layer. To this end, we kept the other layer thicknesses constant (8 nm PTAA, 450 nm perovskite, 20 nm C_{60}, 8 nm BCP, 100 nm copper). We employed measured spectral refractive indices *n* and *k* for all layers under normal incident illumination. The resulting short-circuit current was utilized to numerically solve the modified Shockley-Queisser equation (typical voltage steps are 1 mV) including an ideality factor of 1.5,[9] a shunt resistance of 4000 Ω, a luminescent efficiency of 0.1%[15] a radiative current of 8 x 10^{-20} Acm^{-2} and an internal series resistance of 1.5 Ωcm^2 in addition to the series resistance imposed by the ITO for any given thickness and geometry. Our standard ITO (Automatic Research GmbH, Germany) has a nominal sheet resistance of 15 Ω/sqr with a thickness of 150 nm. We extrapolated the resulting sheet resistance starting from this value.

Data Availability Statement (DAS)

The data that support the plots within this paper and other findings of this study are available from the corresponding author upon reasonable request

References

1. Kojima, A., Teshima, K., Shirai, Y. & Miyasaka, T. Organometal Halide Perovskites as

Visible-Light Sensitizers for Photovoltaic Cells. *J. Am. Chem. Soc.* **131,** 6050–6051 (2009).

2. Kim, H. S. *et al.* Lead iodide perovskite sensitized all-solid-state submicron thin film mesoscopic solar cell with efficiency exceeding 9%. *Sci. Rep.* **2,** 1–7 (2012).
3. Lee, M. M., Teuscher, J., Miyasaka, T., Murakami, T. N. & Snaith, H. J. Efficient Hybrid Solar Cells Based on Meso-Superstructured Organometal Halide Perovskites. *Science (80-.).* **338,** 643–647 (2012).
4. Yang, W. S. *et al.* Iodide management in formamidinium-lead-halide–based perovskite layers for efficient solar cells. *Science (80-.).* **356,** 1376–1379 (2017).
5. Yoshikawa, K. *et al.* Silicon heterojunction solar cell with interdigitated back contacts for a photoconversion efficiency over 26%. *Nat. Energy* **2,** 17032 (2017).
6. Tress, W. Perovskite Solar Cells on the Way to Their Radiative Efficiency Limit - Insights Into a Success Story of High Open-Circuit Voltage and Low Recombination. *Adv. Energy Mater.* **7,** 1602358 (2017).
7. Grancini, G. *et al.* One-Year stable perovskite solar cells by 2D/3D interface engineering. *Nat. Commun.* **8,** 1–8 (2017).
8. Lin, Q., Nagiri, R. C. R., Burn, P. L. & Meredith, P. Considerations for Upscaling of Organohalide Perovskite Solar Cells. *Adv. Opt. Mater.* **5,** 1600819 (2017).
9. Stolterfoht, M. *et al.* Approaching the fill factor Shockley–Queisser limit in stable, dopant-free triple cation perovskite solar cells. *Energy Environ. Sci.* **10,** 1530–1539 (2017).
10. Zhang, W. *et al.* Enhanced optoelectronic quality of perovskite thin films with hypophosphorous acid for planar heterojunction solar cells. *Nat. Commun.* **6,** 10030 (2015).
11. Zheng, X. *et al.* Defect passivation in hybrid perovskite solar cells using quaternary ammonium halide anions and cations. *Nat. Energy* **2,** 17102 (2017).
12. Sherkar, T. S., Momblona, C., Gil-Escrig, L., Bolink, H. J. & Koster, L. J. A. Improving Perovskite Solar Cells: Insights From a Validated Device Model. *Adv. Energy Mater.* **7,** 1602432 (2017).
13. Correa-Baena, J.-P. *et al.* Identifying and suppressing interfacial recombination to achieve high open-circuit voltage in perovskite solar cells. *Energy Environ. Sci.* **10,** 1207–1212 (2017).
14. Tvingstedt, K. *et al.* Removing Leakage and Surface Recombination in Planar Perovskite Solar Cells. *ACS Energy Lett.* **2,** 424–430 (2017).
15. Wolff, C. M. *et al.* Reduced Interface-Mediated Recombination for High Open-Circuit Voltages in CH 3 NH 3 PbI 3 Solar Cells. *Adv. Mater.* **29,** 1700159 (2017).
16. Zheng, X. *et al.* Defect passivation in hybrid perovskite solar cells using quaternary ammonium halide anions and cations. *Nat. Energy* **2,** 17102 (2017).

17. Tan, H. *et al.* Efficient and stable solution-processed planar perovskite solar cells via contact passivation. *Science (80-.).* **355,** 722–726 (2017).
18. Saliba, M. *et al.* Incorporation of rubidium cations into perovskite solar cells improves photovoltaic performance. *Science (80-.).* **354,** 206 (2016).
19. Hou, Y. *et al.* A generic interface to reduce the efficiency-stability-cost gap of perovskite solar cells. *Science (80-.).* **358,** 1192–1197 (2017).
20. Momblona, C. *et al.* Efficient vacuum deposited p-i-n and n-i-p perovskite solar cells employing doped charge transport layers. *Energy Environ. Sci.* **9,** 3456–3463 (2016).
21. Bush, K. A. *et al.* 23.6%-efficient monolithic perovskite/silicon tandem solar cells with improved stability. *Nat. Energy* **2,** 17009 (2017).
22. Albrecht, S. *et al.* Monolithic perovskite/silicon-heterojunction tandem solar cells processed at low temperature. *Energy Environ. Sci.* **9,** 81–88 (2016).
23. Wu, Y. *et al.* Thermally Stable MAPbI3 Perovskite Solar Cells with Efficiency of 19.19% and Area over 1 cm2 achieved by Additive Engineering. *Adv. Mater.* **29,** 1–8 (2017).
24. Palma, A. L. *et al.* Laser-Patterning Engineering for Perovskite Solar Modules With 95% Aperture Ratio. *IEEE J. Photovoltaics* **7,** 1674–1680 (2017).
25. Staub, F. *et al.* Beyond Bulk Lifetimes: Insights into Lead Halide Perovskite Films from Time-Resolved Photoluminescence. *Phys. Rev. Appl.* **6,** 044017 (2016).
26. Richter, J. M. *et al.* Enhancing photoluminescence yields in lead halide perovskites by photon recycling and light out-coupling. *Nat. Commun.* **7,** 13941 (2016).
27. deQuilettes, D. W. *et al.* Photoluminescence Lifetimes Exceeding 8 μs and Quantum Yields Exceeding 30% in Hybrid Perovskite Thin Films by Ligand Passivation. *ACS Energy Lett.* **1,** 438–444 (2016).
28. Ahrenkiel, R. K. Minority-Carrier Lifetime in III–V Semiconductors. *Semicond. Semimetals* **39,** 39–150 (1993).
29. Herz, L. M. Charge-Carrier Mobilities in Metal Halide Perovskites: Fundamental Mechanisms and Limits. *ACS Energy Lett.* **2,** 1539–1548 (2017).
30. deQuilettes, D. W. *et al.* Photo-induced halide redistribution in organic–inorganic perovskite films. *Nat. Commun.* **7,** 11683 (2016).
31. Wurfel, P. The chemical potential of radiation. *J. Phys. C Solid State Phys.* **15,** 3967–3985 (1982).
32. El-Hajje, G. *et al.* Quantification of spatial inhomogeneity in perovskite solar cells by hyperspectral luminescence imaging. *Energy Environ. Sci.* **131,** 6050–6051 (2016).
33. Braly, I. L. & Hillhouse, H. W. Optoelectronic Quality and Stability of Hybrid Perovskites from MAPbI3 to MAPbI2Br Using Composition Spread Libraries. *J. Phys. Chem. C* **120,** 893–902 (2016).
34. Sarritzu, V. *et al.* Optical determination of Shockley-Read-Hall and interface

recombination currents in hybrid perovskites. *Sci. Rep.* **7,** 44629 (2017).

35. Johnston, S. & Unold, T. Correlations of Cu(In, Ga)Se 2 imaging with device performance, defects, and microstructural properties. *J. Vac. Sci. Technol. A Vacuum, Surfaces, Film.* **30,** 4–9 (2012).
36. Bauer, G. H., Gütay, L. & Kniese, R. Structural properties and quality of the photoexcited state in Cu(In1−xGax)Se2 solar cell absorbers with lateral submicron resolution. *Thin Solid Films* **480–481,** 259–263 (2005).
37. Rau, U., Abou-Ras, D. & Kirchartz, T. *Advanced Characterization Techniques for Thin Film Solar Cells*. (Wiley, 2011).
38. Tress, W. *et al.* Predicting the Open-Circuit Voltage of CH 3 NH 3 PbI 3 Perovskite Solar Cells Using Electroluminescence and Photovoltaic Quantum Efficiency Spectra: the Role of Radiative and Non-Radiative Recombination. *Adv. Energy Mater.* **5,** 1400812 (2015).
39. Tvingstedt, K. *et al.* Radiative efficiency of lead iodide based perovskite solar cells. *Sci. Rep.* **4,** 6071 (2014).
40. Kirchartz, T. & Rau, U. Detailed balance and reciprocity in solar cells. *Phys. Status Solidi Appl. Mater. Sci.* **205,** 2737–2751 (2008).
41. Shockley, W. & Queisser, H. J. Detailed Balance Limit of Efficiency of p-n Junction Solar Cells. *J. Appl. Phys.* **32,** 510–519 (1961).
42. Kirchartz, T., Staub, F. & Rau, U. Impact of Photon Recycling on the Open-Circuit Voltage of Metal Halide Perovskite Solar Cells. *ACS Energy Lett.* **1,** 731–739 (2016).
43. Burgelman, M., Nollet, P. & Degrave, S. Modelling polycrystalline semiconductor solar cells. **362,** 527–532 (2000).
44. Lee, J. *et al.* Achieving Large-Area Planar Perovskite Solar Cells by Introducing an Interfacial Compatibilizer. *Adv. Mater.* **29,** 1606363 (2017).
45. Wang, Q., Dong, Q., Li, T., Gruverman, A. & Huang, J. Thin Insulating Tunneling Contacts for Efficient and Water-Resistant Perovskite Solar Cells. *Adv. Mater.* **28,** 6734–6739 (2016).
46. Wu, Y. *et al.* Perovskite solar cells with 18.21% efficiency and area over 1 cm2 fabricated by heterojunction engineering. *Nat. Energy* **1,** 16148 (2016).
47. Green, M. A. *et al.* Solar cell efficiency tables (version 51). *Prog. Photovoltaics Res. Appl.* **26,** 3–12 (2018).
48. Yang, W. S. *et al.* High-performance photovoltaic perovskite layers fabricated through intramolecular exchange. *Science (80-.).* **348,** 1234–1237 (2015).
49. Liu, T. *et al.* High-Performance Formamidinium-Based Perovskite Solar Cells via Microstructure-Mediated δ-to-α Phase Transformation. *Chem. Mater.* **29,** 3246–3250 (2017).

50. Yu, Y. *et al.* Improving the Performance of Formamidinium and Cesium Lead Triiodide Perovskite Solar Cells using Lead Thiocyanate Additives. *ChemSusChem* **9,** 3288–3297 (2016).
51. Delamarre, A., Lombez, L. & Guillemoles, J. F. Contactless mapping of saturation currents of solar cells by photoluminescence. *Appl. Phys. Lett.* **100,** (2012).
52. Burkhard, G. F., Hoke, E. T. & McGehee, M. D. Accounting for Interference, Scattering, and Electrode Absorption to Make Accurate Internal Quantum Efficiency Measurements in Organic and Other Thin Solar Cells. *Adv. Mater.* **22,** 3293–3297 (2010).

Acknowledgements. We thank Pietro Caprioglio for SEM measurements, Lukas Fiedler for laboratory assistance and Frank Jaiser, Florian Dornack and Andreas Pucher for providing measurement and laboratory equipment. P.M. is a Sêr Cymru Research Chair funded by the Welsh European Funding Office (Sêr Cymru II Program) and is formerly an Australian Research Council Discovery Outstanding Researcher Award Fellow. P.L.B is an Australian Research Council Laureate Fellow and S.Z is funded by a Chinese Scholarship Council studentship. We thank Dr Michael Harvey and Brisbane Materials Technology Pty Ltd for the provision of their proprietary anti-reflection coating formulation. J.M. acknowledges Dr. Alex Redinger for fruitful discussions. Support by the joined University Potsdam – HZB graduate school "hypercells" is gratefully acknowledged.

Author contributions. M.S. and C.W. contributed equally to the manuscript. M.S. planned the project together with C.W and D.N., drafted the manuscript and reviewer response, fabricated most cells and films with help of S.Z. and D.R., performed electrical measurements, measured TRPL with C.H. and absolute PL on FAPI cells; C.W. provided important conceptual ideas regarding the identification of the recombination losses, and proposed using PFN and LiF, contributed to device fabrication and TRPL measurements and performed coupled optical and Shockley-Queisser modelling. J.M. performed all hyperspectral PL measurements and performed corresponding data analysis and interpretation; S.Z. helped with device optimization and fabrication. C.H. performed fluence and wavelength dependent TRPL measurements and analysed data; T.U. performed numerical drift diffusion simulations with SCAPS1D and analysed and interpreted the optical measurements. D.R. fabricated certified 1cm2 cells with M.S., and MAPI/FAPI cells and films. D.N. supervised the study, analysed and interpreted all electrical and optical measurements, and contributed to manuscript drafting. All co-authors contributed to data analysis, interpretation and proof reading and addressing reviewer comments.

Competing financial interests. The authors declare no competing financial interests.